Journal of Materials Research and Technology 36 (2025) 8688–8697

Contents lists available at ScienceDirect

Journal of Materials Research and Technology

journal homepage: www.elsevier.com/locate/jmrt

Designing high-capacity hydrogen storage materials: DFT insights into Ca-based complex hydrides MCa M′ H_6 (M = Li, Na; M′ = Co, Rh, Ir)

Asif Hosen [a,*], Ebrahim Nemati-Kande [b], Hanof Dawas Alkhaldi [c], Ahmad A. Mousa [d], Ali Akremi [e], Imed Boukhris [f], Mohammed S. Abu-Jafar [g]

[a] Department of Materials Science and Engineering, Khulna University of Engineering & Technology (KUET), Khulna, 9203, Bangladesh
[b] Department of Physical Chemistry, Chemistry Faculty, Urmia University, Urmia, Iran
[c] Department of Science and Technology, University College at Nairiyah, University of Hafr Al Batin (UHB), Nairiyah, 31981, Saudi Arabia
[d] Middle East University, Amman, 11831, Jordan
[e] Department of Chemistry, Faculty of Science, Northern Border University, Arar, Saudi Arabia
[f] Department of Physics, Faculty of Science, King Khalid University, P.O Box 9004, Abha, Saudi Arabia
[g] Department of Physics, An-Najah National University, Nablus, Palestine

ARTICLE INFO

Keywords:
Complex hydrides
Energy storage
H_2 fuel
Molecular dyamics
Physical properties

ABSTRACT

In this study, density functional theory (DFT) is utilized to explore the structural, electronic, optical, mechanical, thermodynamic, and hydrogen storage properties of MCa M′ H_6 (M = Li, Na; M′ = Co, Rh, Ir) double perovskite-type hydrides for the first time. The structural analysis confirms that all the studied materials crystallize in the cubic phase with space group 216 (F $\bar{4}$3 m). The phonon dispersion analysis confirms that five hydrides – $LiCaRhH_6$, $LiCaIrH_6$, $NaCaCoH_6$, $NaCaRhH_6$, and $NaCaIrH_6$ – demonstrate dynamic stability, while $LiCaCoH_6$ shows the presence of soft modes. Furthermore, *ab initio* molecular dynamic (AIMD) simulations confirmed the thermal stability of the studied materials, showing no structural deformation. All compounds exhibit indirect bandgap semiconductor behavior based on their electronic properties, while a reduction in bandgap is observed when the cationic atom at the M and M′-site in MCa M′ H_6 is substituted. The mechanical properties findings reveal that all the hydrides are mechanically stable and exhibit brittle behavior. We employed the Quasi-Harmonic Debye model to analyze the thermodynamic behavior across different temperatures, and the results align well with fundamental thermodynamic principles. The hydrogen storage characteristics reveal that the studied materials $LiCaCoH_6$, $LiCaRhH_6$, $LiCaIrH_6$, $NaCaCoH_6$, $NaCaRhH_6$, and $NaCaIrH_6$ exhibit storage capacities of 5.40, 3.38, 2.47, 4.72, 3.52, and 2.31 wt%, respectively, demonstrating their potential suitability for hydrogen storage applications. Our findings reveal that $LiCaCoH_6$ is the most suitable material for H_2 storage, as it not only demonstrates the highest storage capacity within the proposed materials but also surpasses the target values established through the US Department of Energy (DOE).

1. Introduction

Energy is essential to our daily lives and is needed to carry out nearly all human activities. Global energy requirement is increasing swiftly because of industrial and economic advancements, with electricity usage in developed nations significantly exceeding the global norm [1]. Generating electricity from fossil fuels releases carbon emissions, contributing to the greenhouse effect [2,3]. The excessive use of fossil resources in homes and its harmful environmental consequence pose a major challenge for engineers to develop eco-friendly energy solutions. Addressing climate change, ensuring energy security, and mitigating the risks associated with resource depletion due to population growth and technological advancement are crucial for the progress of humanity. Promoting renewable energy to have minimal impact on the environment and human life is essential for achieving a solution. Recently, hydrogen economy has appeared as a promising clean and sustainable alternative for transportation and power sectors. Hydrogen stands out as a zero carbon emission fuel with an exceptional gravimetric storage density of 33.3 kWh kg^{-1}, along with easy integration with other energy sources [4]. Hydrogen holds promise to function as a clean fuel in

* Corresponding author.
E-mail address: asif@mse.kuet.ac.bd (A. Hosen).

https://doi.org/10.1016/j.jmrt.2025.05.112
Received 10 April 2025; Accepted 14 May 2025
Available online 16 May 2025

practical applications such as transportation, heating, and cooling, as well as for storing excess electricity [5]. Despite the great potential of large-scale hydrogen energy applications, the absence of safe and affordable solutions for H_2 storage and transportation continues to be a major challenge due to its low density and gaseous nature. At present, hydrogen storage techniques are classified into three main types: compressed as gaseous form, liquified storage at extremely low temperatures, and solid-state storage. Within various storage methods, solid-state metal hydrides (MHs) offer higher gravimetric storage density for hydrogen in a secure, effective, compact, and reversible manner [6–8]. As a result, they are increasingly gaining attention for hydrogen technologies as energy sources.

Recently, perovskite hydride materials have gained considerable interest in the scientific community as potential candidates for fuel in H_2 storage, owing to their high gravimetric energy capacities [9–12]. For ABH_3 perovskites, both experimental and computational investigations have highlighted their significant performance in hydrogen storage applications. According to Bouamrane et al. [13], $NaMgH_3$, recognized for its large bandgap non-conductive nature, may be produced either by direct hydrogenation of Na and Mg blends or through high-energy ball milling. A theoretical study by Mera et al. [14] explored perovskite materials formed with Si and the results revealed that $LiSiH_3$ achieved the highest gravimetric densities of 7.94 wt%, attributed to the minimal mass of the base substrate. In addition to single perovskites, double hydride perovskites also show significant promise for utilization in hydrogen economy. The large and intricate structures of double perovskite materials enable the integration of a greater number of hydrogen atoms. Wang et al. [15] investigated the thermodynamic and kinetic mechanisms involved in H_2 storage process of double perovskite Na_2LiAlH_6. Their findings revealed that decreasing particle size, enhancing crystal defects, and incorporating catalyst doping could effectively enhance the hydrogen absorption and desorption performance. Recently, compounds such as Q_2FeH_6 (Q = Mg, Ca, Sr) [16], Mg_2XH_6 (X = Cr, Mn) [12], A_2LiCuH_6 (A = Be, Mg, Ca, Sr) [17], XGaSiH (X = Sr, Ca, Ba) [18], $KNaX_2H_6$ (X = Mg, Ca) [19], and X_2CaCdH_6 (X = Rb, Cs) [20] have furthermore been studied as promising candidates for hydrogen storage applications.

Inspired by the literature review, this study utilizes first-principles approach to investigate six complex solid-state hydrides, $LiCaCoH_6$, $LiCaRhH_6$, $LiCaIrH_6$, $NaCaCoH_6$, $NaCaRhH_6$, and $NaCaIrH_6$. Among these six systems, $NaCaIrH_6$ was successfully synthesized by Kadir et al. [21] for hydrogen storage through the direct reaction of alkali and alkaline earth binary hydrides with iridium powder. The structural configuration of this material were identified through Guinier − Hägg X-ray and neutron powder diffraction, unveiling a novel cubic lattice arrangement. This structure adopts the F $\overline{4}$3 m space group and resembles the K_2PtCl_6-type structure. However, the physical properties of this material, including its stability, electronic band structure, mechanical behavior, thermodynamic characteristics, and hydrogen storage capacity, remain unexplored. Moreover, for the other five compounds investigated in this study − $LiCaCoH_6$, $LiCaRhH_6$, $LiCaIrH_6$, $NaCaCoH_6$, and $NaCaRhH_6$ − no data is available in the existing literature. Maximizing the potential of hydrogen energy requires an in-depth exploration of material properties, including their crystal structures, hydrogen absorption capacity, electronic behavior, mechanical properties, optical properties, kinetic, and thermodynamic stability. Therefore, in this research, we have examined the aforementioned characteristics of MCa M′ H_6 (M = Li, Na; M′ = Co, Rh, Ir) hydrides to gain a deeper understanding for their potential applications in hydrogen technology. These proposed hydride compounds exhibit a distinctive combination of phase stability, thermodynamic, elastic, and optoelectronic properties, offering valuable insights for developing next-generation hydrogen storage technologies.

2. Computational analysis

First-principles simulations were carried out within the formalism of DFT employing the Quantum ESPRESSO (QE) package [22], which utilizes the projector augmented wave (PAW) method. In all calculations for MCa M′ H_6 (M = Li, Na; M′ = Co, Rh, Ir), the electronic interactions were handled using the Perdew-Burke-Ernzerhof (PBE) approximation under the generalized gradient approximation (GGA) [23,24]. Ultrasoft pseudopotentials from the Garrity − Bennett − Rabe − Vanderbilt (GBRV) library [25] was utilized to perform computations on single-cell unit of the complex hydrides. To obtain a more accurate electronic structure, the HSE06 hybrid functional [26,27], developed by Heyd, Scuseria, and Ernzerhof, was employed. A Monkhorst–Pack k-point mesh of 8 × 8× 8 and a plane-wave energy cutoff of 80 Ry was utilized in simulation process to achieve the most accurate results for all the compounds. During the structural refinement, the material's lattice constants and atomic coordinates were adjusted using the standard DFT GGA-PBE formulation. The simulation identified the lowest-energy, most stable structures through the Broyden − Fletcher − Goldfarb − Shanno (BFGS) algorithm, and all subsequent computations were conducted on the optimized structures. The valence electron configurations for Li, Na, Ca, Co, Rh, Ir, and H are as follows: $1s^2\ 2s^1$ for Li, $2s^2\ 2p^6\ 3s^1$ for Na, $3s^2\ 3p^6\ 4s^2$ for Ca, $3p^6\ 3\,d^7\ 4s^2$ for Co, $4p^6\ 4\,d^8\ 5s^1$ for Rh, $5p^6\ 5\,d^7\ 6s^2$ for Ir, and $1s^1$ for H. The mechanical stability has been assessed through the determination of three elastic constants (C_{11}, C_{12}, C_{44}) via the energy-strain method, which was found in the thermo_pw toolkit and implemented into QE [28]. Various optical characteristics are determined using the real and imaginary parts of the dielectric function through the Kramers-Kronig relations [29]. *Ab initio* molecular dynamic (AIMD) simulations were employed to examine the thermal stability of structures at room temperature (300K). The crystal structure modeling and visualization were carried out employing XCrySDen [30] and VESTA software [31].

3. Results and discussion

3.1. Structural and hydrogen storage properties

The complex hydrides MCa M′ H_6 (M = Li, Na; M′ = Co, Rh, Ir) underwent geometry optimization and crystallized into cubic cells with a F $\overline{4}$3 m (#216) space group orientation [21]. The primitive unit cell of these compounds comprises 9 atoms, whereas the conventional unit cell contains 36 atoms, as presented in Fig. 1. Within the unit cell of MCa M′ H_6 (M = Li, Na; M′ = Co, Rh, Ir), the M^{1+} ion is coordinated by twelve H^{1-} atoms, forming MH_{12} cuboctahedra that are interconnected by sharing their corners with twelve identical MH_{12} unit. The M'^{3+} ion is surrounded by six H^{1-} atoms, forming M′ H_6 octahedra that share their faces with four MH_{12} cuboctahedra and four CaH_{12} cuboctahedra, creating a connected structural network. The optimized lattice constant is obtained through the adjustment of energy in relation to volume using the Birch-Murnaghan equation of state [32,33], as depicted in Fig. 2 (a–f).

$$E(V) = E_0(V) + \frac{BV}{B'}\left[\frac{\left(\frac{V_0}{V}\right)^{B'}}{B'-1} + 1\right] - \frac{BV_0}{B'-1} \quad (1)$$

The calculated lattice constants for $LiCaCoH_6$, $LiCaRhH_6$, $LiCaIrH_6$, $NaCaCoH_6$, $NaCaRhH_6$, and $NaCaIrH_6$ are 6.78 Å, 7.00 Å, 7.02 Å, 6.99 Å, 7.21 Å, and 7.22 Å, respectively. Notably, the lattice constant of $NaCaIrH_6$ closely aligns with previous experimental results (a = 7.23 Å) [21], confirming the reliability of our calculations. Replacing Co atoms with Rb and Ir increases the atomic radii, which in turn alters the physical characteristics of these compounds, including volume (V), bulk modulus (B), and ground state energy (E_0), among others. The detailed

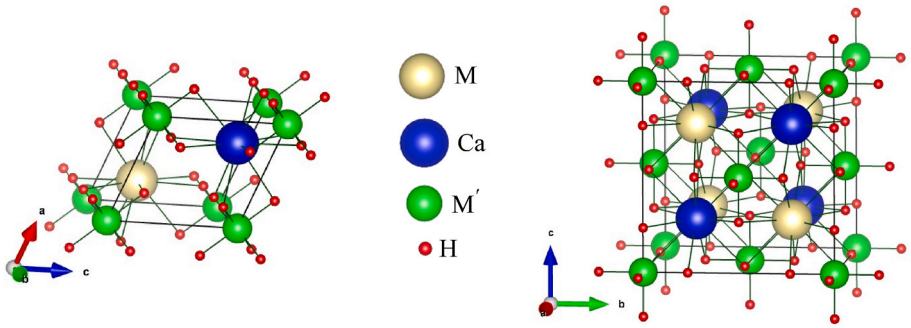

Fig. 1. Side view of MCa M′ H_6 (M = Li, Na; M′ = Co, Rh, Ir) hydrides showcasing both primitive and conventional unit cells. The M, Ca, M′ and H atoms are represented by yellow, blue, green and red spheres, respectively.

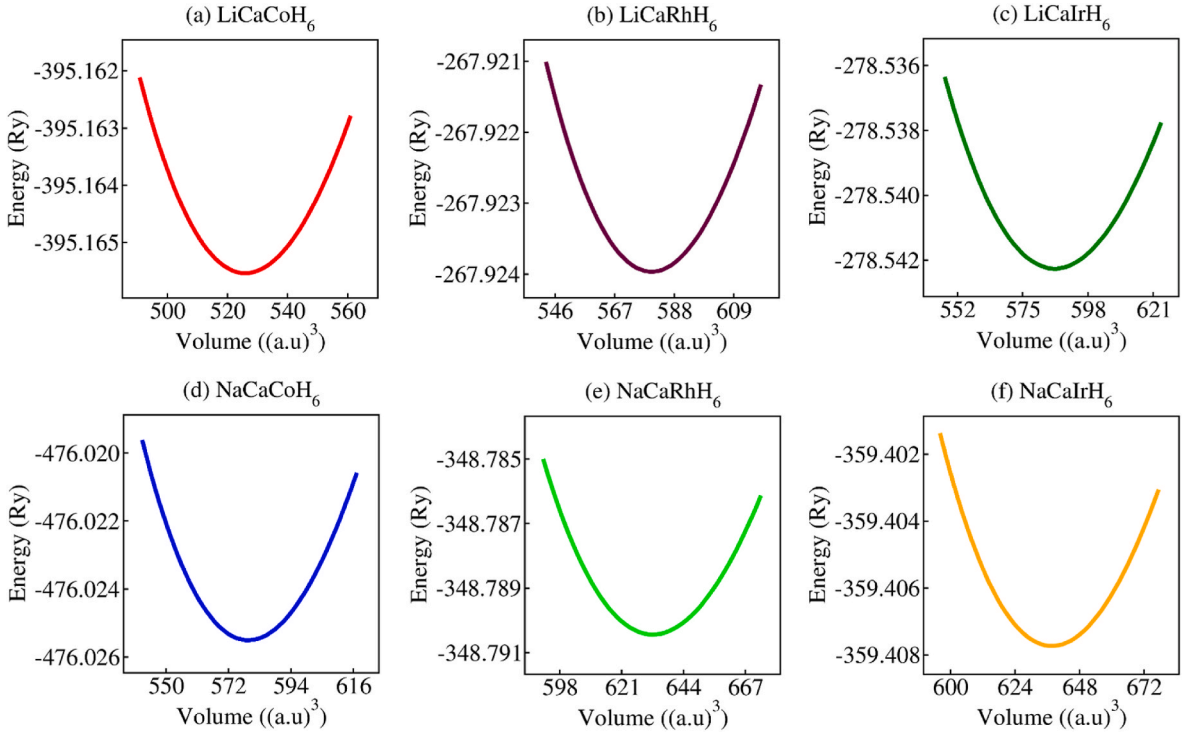

Fig. 2. The optimized energy-volume graphs of MCa M′ H_6 (M = Li, Na; M′ = Co, Rh, Ir) hydrides.

information about the aforementioned properties of the unit cell are presented in Table 1.

To assess the applicability of MCa M′ H_6 (M = Li, Na; M′ = Co, Rh, Ir) compounds as an efficient material fuel for hydrogen economy, the gravimetric storage capacity ($C_{wt\%}$) is a crucial parameter analyzed through theoretical calculations. $C_{wt\%}$ refers to the highest quantity of H_2 that a material can store per unit mass, and it increases as the hydrogen content in the material increases [34,35]. To calculate $C_{wt\%}$, we utilized Eq. (2), where $\frac{H}{M}$ represents the hydrogen to host material ratio, while m_{Host} and m_H denote the molar masses of the host material and hydrogen atoms, respectively.

$$C_{wt\%} = \left(\frac{\left(\frac{H}{M}\right) m_H}{m_{Host} + \left(\frac{H}{M}\right) m_H} \times 100 \right) \% \tag{2}$$

Based on the computed gravimetric densities, it is determined that $LiCaCoH_6$ has the highest $C_{wt\%}$ of 5.40 wt%, followed by $NaCaCoH_6$ at 4.72 wt%, $LiCaRhH_6$ at 3.88 wt%, $LiCaRhH_6$ at 3.52 wt%, $LiCaIrH_6$ at 2.47 wt%, and $NaCaIrH_6$ at 2.31 wt%. The U.S. DOE has established a benchmark of 4.5 wt% for the gravimetric capacity of hydrides used in rechargeable equipment [35,36]. So, $C_{wt\%}$ value of two materials, $LiCaCoH_6$ and $NaCaCoH_6$, surpasses the target established by the U.S. DOE, indicating that they are outstanding candidates for use in hydrogen technology as fuel. Conversely, the $C_{wt\%}$ value of the other four materials – $LiCaRhH_6$, $NaCaRhH_6$, $LiCaIrH_6$, and $NaCaIrH_6$ – falls short of the target value. However, the storage capacity of these hydrides can

Table 1
The optimized lattice parameters (a, Å), volume (V, a.u.^{3}), bulk modulus (B, GPa), pressure derivative of bulk modulus (B'), minimum energy (E_0, Ry), and H_2 storage capacity ($C_{wt\%}$, wt%) of MCa M′ H_6 (M = Li, Na; M′ = Co, Rh, Ir).

Materials	a	V	B	B'	E_0	$C_{wt\%}$
$LiCaCoH_6$	6.78	525.92	46.71	3.77	− 395.16	5.40
$LiCaRhH_6$	7.00	579.98	43.72	3.38	− 267.92	3.88
$LiCaIrH_6$	7.02	586.30	45.90	3.65	− 278.54	2.47
$NaCaCoH_6$	6.99	578.98	43.73	4.05	− 476.02	4.72
$NaCaRhH_6$	7.21	632.56	41.01	3.92	− 348.79	3.52
$NaCaIrH_6$	7.22 this work	637.67	43.01	4.03	− 359.41	2.31
	7.23 exp. [21]					

be enhanced through doping [37–39] or by employing thin films and nanostructures, which provide greater surface areas and higher storage capacities compared to their bulk forms [40].

3.2. Stability

Computing phonon dispersion characteristics offers important informations into the dynamic stability of compounds by uncovering the vibrational behavior of atoms within the crystal framework. Imaginary frequencies in phonon curves signify dynamic instability in a material, while their absence indicates stability. Fig. 3(a–f) presents the computed phonon dispersion curves for the complex hydrides, showing no negative frequency modes for five materials – $LiCaRhH_6$, $LiCaIrH_6$, $NaCaCoH_6$, $NaCaRhH_6$, and $NaCaIrH_6$ – indicating their stability. Only $LiCaCoH_6$ exhibits a slight negative frequency value, as shown in Fig. 3 (a). All phonon calculations in this study were conducted using the primitive unit cell. The instability of $LiCaCoH_6$ may be overhauled in future research by simulating a larger number of atoms with a supercell approach. Despite the previous discussions on phonon spectra, these calculations are typically performed at absolute zero temperature, relying on the harmonic approximation while neglecting interactions and energy transfer among lattice vibrations. However, considering lattice anharmonicity, which includes thermal expansion and conduction at higher temperatures, can soften lattice vibrations and result in temperature-dependent dynamic stability. Recently, numerous studies have shown that a compound can remain stable at higher temperatures, including ambient conditions, despite exhibiting imaginary frequencies in its phonon spectrum at 0 K [41–44].

Thus, to reasonably assess the thermal stability of these hydrides over a specific temperature range, we employ *ab initio* molecular dynamic (AIMD) simulations at 300K, running for a total of 5 ps with a timestep of 1 fs. As shown in Fig. 4(a–f), the total energy vibration exhibits smaller fluctuations over time, indicating that all the proposed materials are generally thermodynamically stable at room temperature. These results indicate the high thermal stability of the six MCa M′ H_6 (M = Li, Na; M′ = Co, Rh, Ir) structures.

3.3. Electronic properties

To comprehend the electronic properties of MCa M′ H_6 (M = Li, Na; M′ = Co, Rh, Ir) solid state hydrides, it is crucial to examine both the band structure (BS) and the density of states (DOS) at the equilibrium lattice constant. These computations, carried out along the high-symmetry directions of the first Brillouin zone (BZ), utilized the GGA-PBE (red solid lines) and HSE06 (blue dashed lines) methods, as illustrated in Fig. 5(a–f), offering critical insights into the electronic properties. The Fermi level, denoted as E_F, marks the boundary between the conduction band (CB) and the valence band (VB). Fig. 5 displays the band structure profile of the studied materials, where it is evident that the dispersion curves in the CB do not overlap with those in the VB using both methods, indicating its semimetallic nature. As presented in Fig. 5, the indirect band gap (at the X–U high-symmetry point) for $LiCaCoH_6$, $LiCaRhH_6$, $LiCaIrH_6$, $NaCaCoH_6$, $NaCaRhH_6$, and $NaCaIrH_6$ is calculated to be 2.01 (4.63) eV, 2.97 (4.62) eV, 3.41 (4.84) eV, 1.98 (4.62) eV, 3.07 (4.56) eV, and 3.36 (4.77) eV, respectively, using the GGA-PBE (HSE06) approximation. So, it is evident that the standard DFT – PBE functional consistently underestimates the electronic structure, particularly the band gap. Nevertheless, despite this underestimation, the results indicate that the dispersion of the VB and CB, as well as the nature of the band gap, produce consistent outcomes with HSE06 hybrid functional.

The atomic contributions to band formation and the peaks in the density of states (DOS) plot are clarified by presenting the atomic DOS plot, as shown in Fig. 6(a–f). By examining the atom-projected DOS, we observed that the VBs are primarily influenced by H-s, Ca-d, M′-p and M′-d states, with small contributions from the M-site cations, whereas the CBs are mainly shaped by Ca-d and M′-d states, with minimal input from the H-s and M-site cations. Additionally, we noted that the VBM is defined by H-s and M′-d states, while the CBM exhibits features of Ca-d states, as illustrated in Fig. 6. The total density of states (TDOS), which represents the various energy levels available for electrons, has also been plotted in Fig. 6. The TDOS for all hydrides reveals a distinct bandgap.

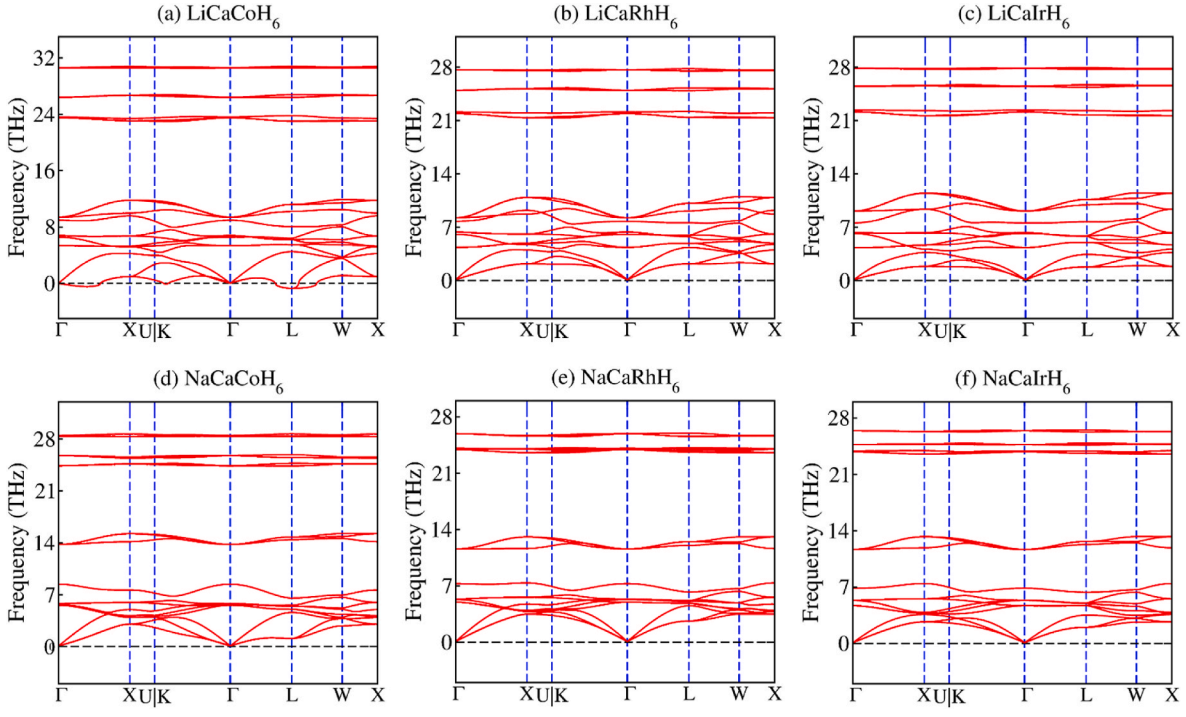

Fig. 3. Phonon band structure for (a) $LiCaCoH_6$, (b) $LiCaRhH_6$, (c) $LiCaIrH_6$, (d) $NaCaCoH_6$, (e) $NaCaRhH_6$, and (f) $NaCaIrH_6$.

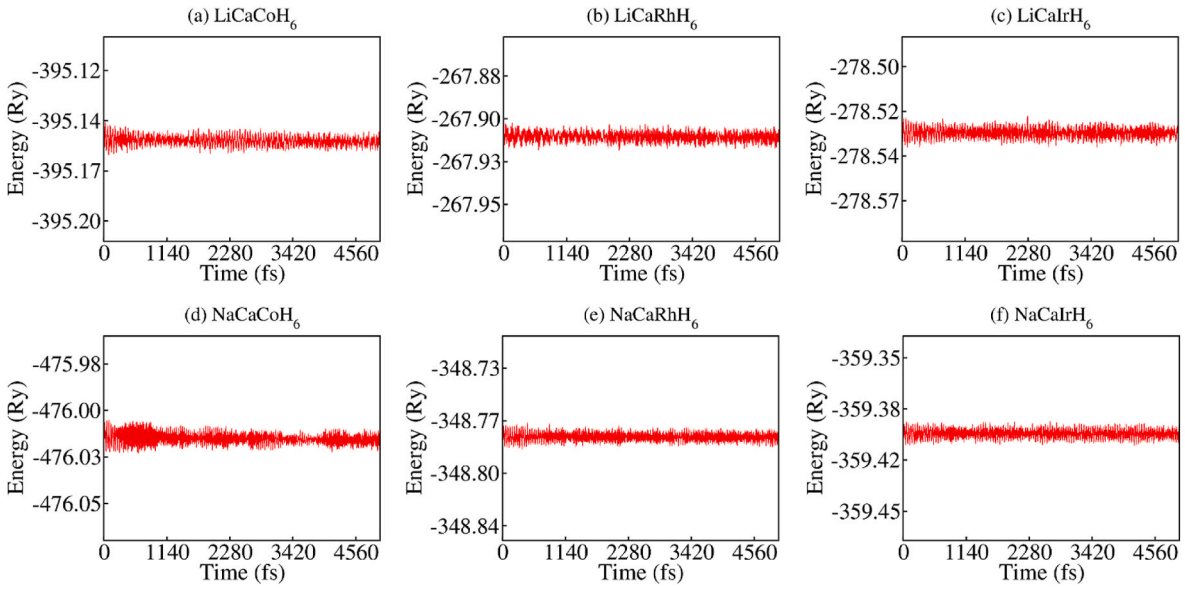

Fig. 4. Total energy fluctuation at 300 K estimated in *ab initio* molecular dynamic (AIMD) simulations of MCa M′ H_6 (M = Li, Na; M′ = Co, Rh, Ir) hydrides.

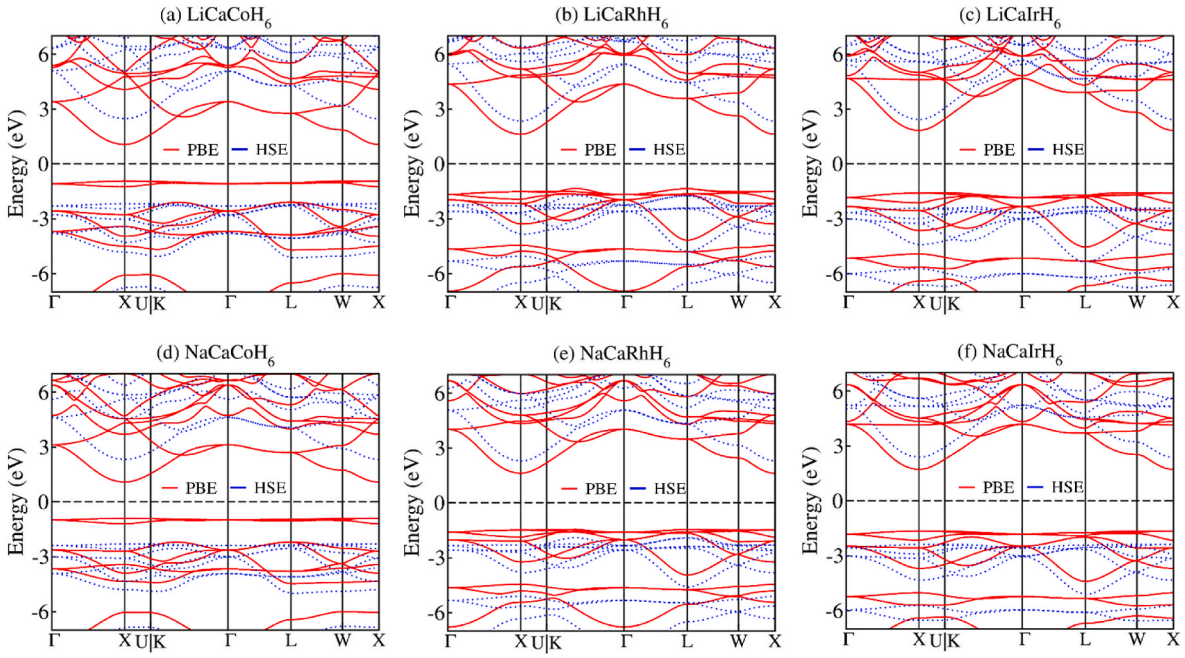

Fig. 5. Band structure of cubic MCa M′ H_6 (M = Li, Na; M′ = Co, Rh, Ir) hydrides in GGA (solid red lines), and HSE06 (blue dashed lines). The labeling of high symmetry points in the Brillouin zone follows the conventions outlined in Refs. [58,59]. The horizontal black dashed marker represents the Fermi level (E_F).

3.4. Optical properties

Optical properties enable the evaluation of how a material reacts to an incoming electromagnetic (EM) wave, facilitating the exploration of potential applications. The optical characteristics of a material are vital for advancements in optoelectronics and solar cell technology [11,45]. The interaction between electrons and photons in the studied materials is crucial for comprehending the knowledge of optical properties. Electrons typically transition to the conduction band following successful collisions, facilitating the transfer of energy from photons to electrons [46]. The frequency-dependent dielectric function (DF), $\varepsilon(\omega)$, as given in Eq. (3), which consists of real part, $\varepsilon_1(\omega)$, and an imaginary part, $\varepsilon_2(\omega)$, is widely used to assess optical characteristics. The real part, $\varepsilon_1(\omega)$, is derived from $\varepsilon_2(\omega)$ through the Kramers-Kronig relation, as shown in Eq. (4), while the imaginary part, $\varepsilon_2(\omega)$, is determined using Eq. (5).

$$\varepsilon(\omega) = \varepsilon_1(\omega) + i\varepsilon_2(\omega) \tag{3}$$

$$\varepsilon_1(\omega) = 1 + \frac{2}{\pi} P \int_0^{\infty} \frac{\omega' \varepsilon_2(\omega')}{\omega'^2 - \omega^2} d\omega' \tag{4}$$

P is the Cauchy integral.

$$\varepsilon_2(\omega) = \frac{(4\pi^2 e^2)}{(\pi\omega^2 m^2)} \Sigma_{ij} \int_{BZ}^{\infty} [M_{ij}(k)]^2 f_i(1 - f_j)\, \delta[E_f - E_i - \omega] d^3k \tag{5}$$

Furthermore, by utilizing the dispersion of the real and imaginary portions of DF, various optical parameters – including absorption coeffi-

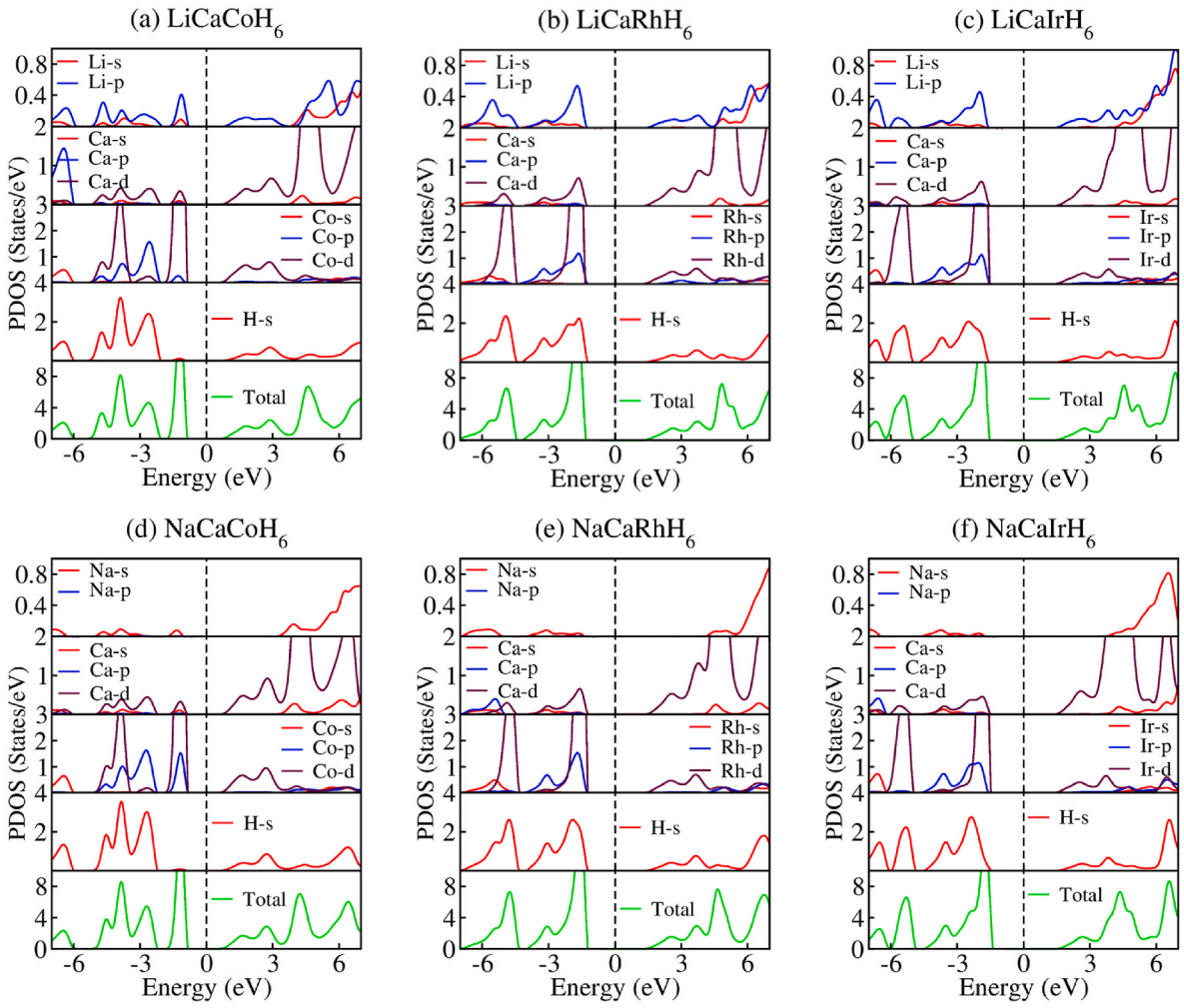

Fig. 6. Computed density of states (DOS) of MCa M′ H_6 (M = Li, Na; M′ = Co, Rh, Ir). The vertical black dashed marker represents the Fermi level (E_F).

cient, reflectivity, refractive indices, and the extinction coefficient – can be determined using the following formulas.

$$\alpha(\omega) = \sqrt{2\omega}\left[-\varepsilon_1(\omega) + \sqrt{\varepsilon_1^2(\omega) + \varepsilon_2^2(\omega)}\right]^{1/2} \tag{6}$$

$$R(\omega) = \left|\frac{\sqrt{\varepsilon(\omega)} - 1}{\sqrt{\varepsilon(\omega)} + 1}\right|^2 \tag{7}$$

$$n(\omega) = \left[\frac{\sqrt{\varepsilon_1^2(\omega) + \varepsilon_2^2(\omega)} + \varepsilon_1(\omega)}{2}\right]^{1/2} \tag{8}$$

$$k(\omega) = \left[\frac{\sqrt{\varepsilon_1^2(\omega) + \varepsilon_2^2(\omega)} - \varepsilon_1(\omega)}{2}\right]^{1/2} \tag{9}$$

Fig. 7(a) and (b) presents $\varepsilon_1(\omega)$, and $\varepsilon_2(\omega)$, parts of the DF for MCa M′ H_6 (M = Li, Na; M′ = Co, Rh, Ir) hydrides. $\varepsilon_1(\omega)$, describes the material's capacity to store energy within an electric field, $\varepsilon_2(\omega)$, represents its ability to either retain or dissipate energy [47]. The actual component of the DF, $\varepsilon_1(\omega)$, for all analyzed materials, as presented in Fig. 7(a), exhibits static values of 4.84 for $LiCaCoH_6$, 5.01 for $LiCaRhH_6$, 4.76 for $LiCaIrH_6$, 4.48 for $NaCaCoH_6$, 4.65 for $NaCaRhH_6$, and 4.47 for $NaCaIrH_6$. These values reflect different degrees of polarization, with $LiCaRhH_6$ exhibiting the highest static dielectric response and $NaCaIrH_6$ the lowest. Negative values of $\varepsilon_1(\omega)$ are observed within certain energy ranges for each hydride. These negative values indicate plasma-like behavior, where the incident EM field oscillates at a frequency higher than the solid's plasma frequency, preventing electrons from effectively responding to the external electric field and causing the substance to behave as a ideal reflector. This results in reduced transmission and increased optical loss in these energy regions, which is essential for understanding the optical and electromagnetic characteristics of these hydrides, highlighting their potential use in reflective coatings or energy storage devices [48]. Furthermore, the peak values for $\varepsilon_2(\omega)$ are observed at 7.65 for $LiCaCoH_6$ at 5.02 eV, 7.80 for $LiCaRhH_6$ at 5.14 eV, 7.76 for $LiCaIrH_6$ at 5.81 eV, 7.52 for $NaCaCoH_6$ at 5.05 eV, 8.11 for $NaCaRhH_6$ at 5.04 eV, and 8.01 for $NaCaIrH_6$ at 5.70 eV, as found in Fig. 7(b), highlighting the energy ranges where these materials exhibit the strongest light absorption.

The absorption coefficient provides insight into a material's capacity to absorb photons, where a larger value signifies more efficient photon absorption. The absorption coefficient $\alpha(\omega)$ for MCa M′ H_6 (M = Li, Na; M′ = Co, Rh, Ir) has been computed using Eq. (6) and is presented in Fig. 7(c). Our analysis shows that all the investigated materials exhibit a generally increasing trend with minor fluctuations. The principal absorption peak values observed are 13.01 × 10^5 cm^{-1} at 11.20 eV for $LiCaCoH_6$, 15.98 × 10^5 cm^{-1} at 10.31 eV for $LiCaRhH_6$, 17.80 × 10^5 cm^{-1} at 9.95 eV for $LiCaIrH_6$, 12.69 × 10^5 cm^{-1} at 10.74 eV for $NaCaCoH_6$, 14.95 × 10^5 cm^{-1} at 9.53 eV for $NaCaRhH_6$, and 16.29 × 10^5 cm^{-1} at 9.55 eV for $NaCaIrH_6$, respectively. Also, the curves start at a specific photon energy, confirming the existence of an energy band gap, which aligns with the electronic properties analysis. We also examined the frequency-dependent reflectivity $R(\omega)$ of the target

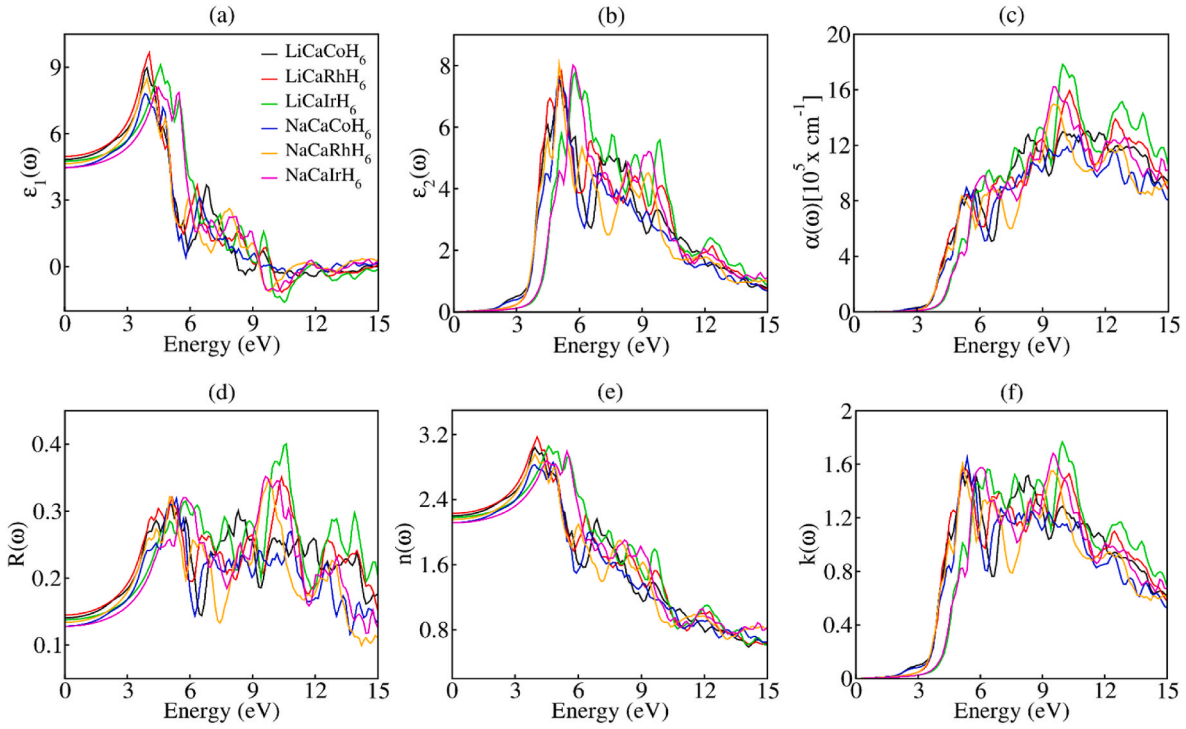

Fig. 7. Calculated spectra of (a&b) dielectric function, (c) absorption, (d) reflectivity, (e) refractive index, and (f) extinction coefficient of MCa M′ H_6 (M = Li, Na; M′ = Co, Rh, Ir) hydrides against photon energy.

materials, and the corresponding graphs are displayed in Fig. 7(d). The peak reflectivity values are observed at 0.31 for $LiCaCoH_6$ at 5.02 eV, 0.35 for $LiCaRhH_6$ at 10.44 eV, 0.40 for $LiCaIrH_6$ at 10.62 eV, 0.32 for $NaCaCoH_6$ at 5.37 eV, 0.34 for $NaCaRhH_6$ at 9.86 eV, and 0.35 for $NaCaIrH_6$ at 9.69 eV.

The optical constants $n(\omega)$ and $k(\omega)$, derived from Eqs. (8) and (9), are depicted in Fig. 7(e) and **(f)**, respectively, exhibiting trends that align with $\varepsilon_1(\omega)$ and $\varepsilon_2(\omega)$. The static refractive index values for $LiCaCoH_6$, $LiCaRhH_6$, $LiCaIrH_6$, $NaCaCoH_6$, $NaCaRhH_6$, and $NaCaIrH_6$ are 2.20, 2.23, 2.18, 2.12, 2.16, and 2.11, respectively, all indicating a refractive index higher than 1. This suggests that light slows down as it passes through a medium composed of these hydrides, causing dispersion, since light travels more slowly in these compounds compared to a vacuum [48]. Notably, $k(\omega)$ starts at zero for minimal photon energy and begins to rise at certain values of photon energy. The maximum values of 1.55 at 5.51 eV, 1.59 at 5.16 eV, 1.76 at 9.97 eV, 1.66 at 5.39 eV, 1.62 at 5.14 eV, and 1.69 at 9.54 eV for $LiCaCoH_6$, $LiCaRhH_6$, $LiCaIrH_6$, $NaCaCoH_6$, $NaCaRhH_6$, and $NaCaIrH_6$, respectively, indicate effective interaction with incident photons [19]. To the best of our knowledge, we first investigated the optical dispersions of double perovskite-type MCa M′ H_6 (M = Li, Na; M′ = Co, Rh, Ir). These properties provide essential knowledge about their performance in practical applications and serve as motivation for researchers to conduct further experiments in this field.

3.5. Elastic and mechanical properties

The elastic and mechanical behavior of a material are defined by its elastic constants, which measure the correlation between applied stress and strain. These constants dictate how a substance deforms when subjected to external forces and its ability to return to its original shape afterward [49]. In our research, we performed an extensive evaluation of the elastic and mechanical properties of the studied compounds, encompassing key parameters like the elastic constants (C_{11}, C_{12}, and C_{44}), shear modulus (G), bulk modulus (B), Young's modulus (E), and other pertinent properties. Since the hydride materials being studied exhibit cubic symmetry, their mechanical behavior can be sufficiently expressed using just three elastic constants: C_{11}, C_{12}, and C_{44}. It is essential that the elastic constants fully satisfy Born-Huang criterion [50] in Eq. (10), requiring all calculated elastic constants must have positive values, as failure to meet this criterion prevents further evaluation of the compound's mechanical properties.

$$C_{11} > 0, C_{11} - C_{12} > 0, C_{11} + 2C_{12} > 0, C_{11} > B_0 > C_{12} \tag{10}$$

As shown in Table 2, all the hydride materials meet the aforementioned Born's stability criteria with their three independent elastic constants (C_{11}, C_{12}, and C_{44}), confirming their mechanical stability and indicating excellent stability during hydrogenation and dehydrogenation processes. As shown in Table 2, the C_{11} values for the studied compounds follow this sequence: $LiCaCoH_6 > NaCaCoH_6 > LiCaRhH_6 > LiCaIrH_6 > NaCaRhH_6 > NaCaIrH_6$. The elastic constant C_{11} value is highest for $LiCaCoH_6$ (107.02 GPa) and lowest for $NaCaIrH_6$ (82.38 GPa), indicating that $LiCaCoH_6$ has the strongest resistance to longitudinal deformation, making it the hardest material studied, while $NaCaIrH_6$ is relatively soft due to its low resistance to such deformation.

Furthermore, these evaluated elastic constants are utilized to calculate the key mechanical properties of the compounds in title by applying the following standard formulas:

$$B = B_v = B_R = \frac{(C_{11} + 2C_{12})}{3} \tag{11}$$

Table 2
Elastic constant (C_{ij}, GPa) of MCa M′ H_6 (M = Li, Na; M′ = Co, Rh, Ir).

Materials	C_{11}	C_{12}	C_{44}
$LiCaCoH_6$	107.02	29.05	39.12
$LiCaRhH_6$	90.05	22.22	36.45
$LiCaIrH_6$	88.35	23.09	37.30
$NaCaCoH_6$	96.16	22.32	38.82
$NaCaRhH_6$	83.04	19.43	35.37
$NaCaIrH_6$	82.38	21.76	36.35

$$B_H = \frac{(B_R + B_v)}{2} \tag{12}$$

$$G_v = \frac{C_{11} - C_{12} + 3C_{44}}{5} \tag{13}$$

$$G_R = \frac{5C_{44}\,(C_{11} - C_{12})}{4C_{44} + 3(C_{11} - C_{12})} \tag{14}$$

$$G_H = \frac{(G_R + G_v)}{2} \tag{15}$$

$$Y = \frac{9BG}{3B + G} \tag{16}$$

$$\nu = \frac{3B - 2G}{2(3B + G)} \tag{17}$$

Using the aforementioned equations, the determined parameters are presented in Table 3. The bulk modulus (B) serve as a key parameter in evaluating mechanical properties, as it measures a material's ability to withstand volumetric variations when exposed to increased external pressure [51]. The calculated results reveal that $LiCaCoH_6$ has a higher B value (55.04 GPa) compared to other materials, indicating its greater resistance to volumetric changes under external stress. Furthermore, the shear modulus (G) quantifies a material's ability to resist shape deformation [52], and $LiCaCoH_6$'s higher G value compared to the other five hydrides indicates that it is more resistant to shape irregularities than the rest. Another crucial parameter is Young's modulus (E), which quantifies a material's ability to stretch or compress when a force is applied [53]. The obtained results for E suggest that $LiCaCoH_6$ is the stiffest material, exhibiting the least tendency to stretch or compress under applied forces.

To evaluate the ductility/brittleness of materials, three key parameters serve as crucial indicators: Poisson's ratio (ν), Pugh's ratio (B/G), and Cauchy pressure (C_p). Firstly, Poisson's ratio (ν), defined as the positive ratio of transverse to axial strain and calculated using Eq. (17), indicates ductility if it exceeds 0.26, whereas a value below 0.26 signifies brittleness. Secondly, The Pugh ratio (B/G), calculated as the bulk modulus (B) divided by the shear modulus (G), is a key parameter for assessing ductility and brittleness, with values below 1.75 signaling brittleness, and values above 1.75 indicating ductility. Finally, Cauchy pressure (C_p), defined as the difference between the elastic constants C_{12} and C_{44}, also acts as a gauge for material's mechanical behavior. A positive C_p value signifies ductility, allowing significant plastic deformation before fracture, whereas a negative value indicates brittleness, making the material prone to fracture under stress with minimal deformation. As shown by the computed values in Table 3 and the visualization of ν and B/G in Fig. 8(a–b), all the materials examined in this study are classified as brittle based on the aforementioned criteria ($\nu < 0.26$, $B/G < 1.75$, $C_p < 0$).

The classification of materials as isotropic or anisotropic depends on the anisotropy factor (A), which is calculated using the following Zener formula [54]:

$$A = \frac{2C_{44}}{C_{11} - C_{12}} \tag{18}$$

Table 3
Mechanical attributes of MCa M′ H_6 (M = Li, Na; M′ = Co, Rh, Ir).

Materials	B	G	E	$C_p = C_{12} - C_{44}$	ν	B/G	A
$LiCaCoH_6$	55.04	39.06	94.77	− 10.07	0.21	1.41	1.01
$LiCaRhH_6$	44.83	35.41	84.09	− 14.23	0.19	1.27	1.07
$LiCaIrH_6$	44.84	35.36	84.00	− 14.21	0.19	1.27	1.14
$NaCaCoH_6$	46.93	38.05	89.86	− 16.50	0.18	1.23	1.05
$NaCaRhH_6$	40.63	38.90	79.70	− 15.94	0.17	1.04	1.11
$NaCaIrH_6$	41.97	33.80	79.94	− 14.59	0.18	1.24	1.20

An A value of 1 signifies isotropic behavior, while values deviating from 1, whether higher or lower, indicate anisotropy. As listed in Table 3, the obtained A values for $LiCaCoH_6$, $LiCaRhH_6$, $LiCaIrH_6$, $NaCaCoH_6$, $NaCaRhH_6$, and $NaCaIrH_6$ are equal to 1.01, 1.07, 1.14, 1.05, 1.11, and 0.20, respectively, proving their anisotropy. So, our analysis clearly indicates that the anisotropic behavior becomes more pronounced as the atomic weight of the hydride increases or as the atomic radius expands, moving from Co to Ir or Li to Na.

3.6. Thermodynamic properties

Determining thermodynamic properties is crucial for comprehending how materials respond to temperatures that are different from their standard state. This study utilizes the quasi-harmonic Debye model to analyze the thermodynamic behavior of MCa M′ H_6 (M = Li, Na; M′ = Co, Rh, Ir) hydrides across a temperature range of 0–800K, within the framework of GGA approximation. Entropy (S) quantifies the randomness and disorder within a system, and analyzing its variation with temperature allows us to assess the level of uncertainty or disruption in solids. Fig. 9(a–f) depicts the correlation between entropy (S) and temperature (T) within the range of 0–800K, showing that S is zero at 0K and increases exponentially with rising the temperature, indicating greater disorder within the system at higher temperatures for all hydrides. Temperature enhances thermal vibrations, causing particles in a material to move more energetically as it rises [55]. The constant-volume heat capacity (C_v) is a key thermodynamic properties that quantifies a material's capacity to absorb heat while maintaining a fixed volume [49]. Fig. 9 presents the changes in C_V with temperature for MCa M′ H_6 (M = Li, Na; M′ = Co, Rh, Ir), showcasing significant patterns in their thermal behavior. Below 350K, C_V shows a significant temperature dependence, adhering to a T^3 relationship as described by the Debye T^3 law [49]. When the temperature surpasses 350K, C_V increases at a slower rate, gradually approaching the Dulong – Petit limit [56], which represents the maximum contribution of atomic vibrations to heat capacity at elevated temperatures. Also, as shown in Fig. 9, as temperature increases, the energy of all systems rises due to intensified atomic vibrations. Conversely, the free energy of these materials declines, highlighting their strong thermodynamic stability at elevated temperatures [57].

4. Conclusion

The structural, optoelectronic, mechanical, thermodynamic, and hydrogen storage performance of the MCa M′ H_6 (M = Li, Na; M′ = Co, Rh, Ir) hydride material, with different cation site configurations, were analyzed using QE program. Firstly, for establishing the ground-state structural parameters, the total energy was fitted relative to the unit cell volume, leading to the conclusion that all six materials are stable in cubic cells with F $\overline{4}$3 m (#216) space group orientation. We also observe that the calculated lattice parameter and band gap of $NaCaIrH_6$ align well alongside experimental data documented within published studies. The phonon dispersion curves show no presence of negative frequencies, verifying the dynamical stability of all five materials, whereas $LiCaCoH_6$ exhibits a few imaginary frequencies. Furthermore, a comprehensive AIMD simulation analysis confirms the complete stability of all studied materials, as indicated by minimal fluctuations in equilibrium energy, eliminating concerns regarding structural reliability for real-world applications. The computed elastic constants C_{ij} and related parameters, including B/G, ν, C_p, and A, indicate that these studied materials exhibit brittle behavior under ambient conditions and lacks significant elastic isotropy. The heat capacity (C_v) of all materials follows the same trend, increasing with temperature and approaching the Dulong-Petit limit at high temperatures. The hydrogen storage analysis shows that $LiCaCoH_6$ and $NaCaCoH_6$ exhibit excellent gravimetric capacities of 5.41 and 4.73 wt%, respectively, while $LiCaRhH_6$, $LiCaIrH_6$, $NaCaRhH_6$, and $NaCaIrH_6$

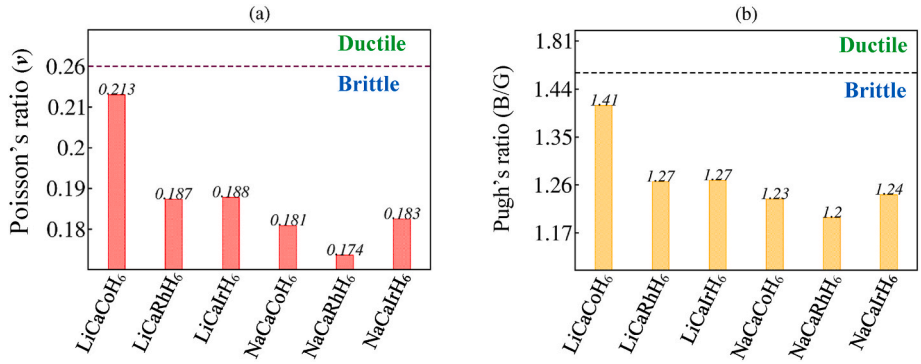

Fig. 8. Computed mechanical parameters (a) ν [Poisson's ratio], (b) B/G [Pugh ratio] for MCa M′ H_6 (M = Li, Na; M′ = Co, Rh, Ir) hydrides.

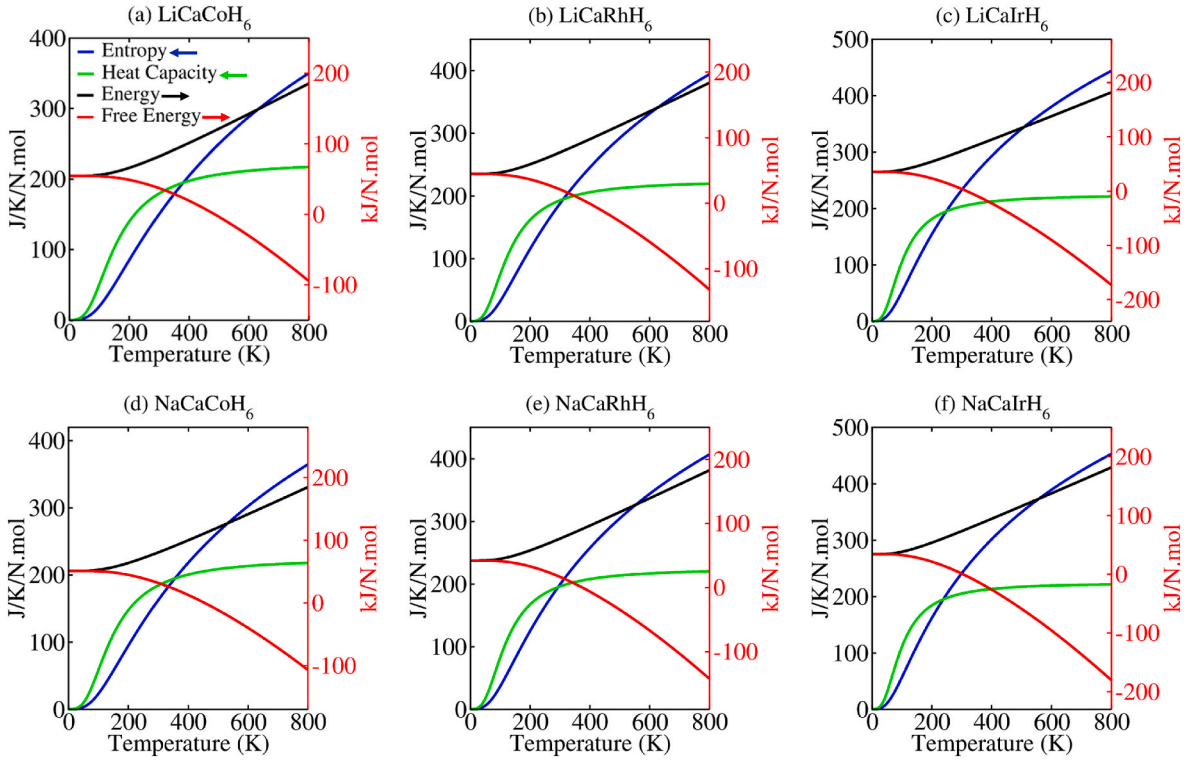

Fig. 9. The change in (a) entropy, (b) heat capacity, (c) energy, and (d) free energy against the temperature of MCa M′ H_6 (M = Li, Na; M′ = Co, Rh, Ir).

demonstrate moderate storage capacities of 3.88, 2.47, 3.52, and 2.31 wt%, respectively. Overall, the outcomes of this research a provide significant guide for experimentalists in synthesizing these hydride materials for hydrogen fuel applications. Also, this research offer a foundation for theoreticians to further optimize the gravimetric storage capacities of the investigated materials.

Declaration of competing interest

The authors declare that they have no known competing financial interests or personal relationships that could have appeared to influence the work reported in this paper.

Acknowledgements

The authors thank the Deanship Research and Graduate Studies at King Khalid University, Saudi Arabia for funding this work through the Large Groups Project under Grant Number (RGP.2/293/46). The authors extend their appreciation to the Deanship of Scientific Research at Northern Border University, Arar, KSA, for funding this research work through the project number NBU-FFR-2025-2246-02.

References

[1] Sorgulu F, Dincer I. A renewable source based hydrogen energy system for residential applications. Int J Hydrogen Energy 2018;43:5842–51.
[2] Canyurt OE, Ozturk HK. Application of genetic algorithm (GA) technique on demand estimation of fossil fuels in Turkey. Energy Policy 2008;36:2562–9.
[3] Bakay MS, Ağbulut Ü. Electricity production based forecasting of greenhouse gas emissions in Turkey with deep learning, support vector machine and artificial neural network algorithms. J Clean Prod 2021;285:125324.
[4] Shao L, Lin X, Yang X, Zhao Y, Zhang J, Cheng T, et al. Magnesium-based hydrogen storage tanks: a review of research, development and simulation models. Renew Sustain Energy Rev 2025;211:115332.
[5] Moradi R, Groth KM. Hydrogen storage and delivery: review of the state of the art technologies and risk and reliability analysis. Int J Hydrogen Energy 2019;44:12254–69.
[6] Prabhukhot PR, Wagh MM, Gangal AC. A review on solid state hydrogen storage material. Advances in Energy and Power 2016;4(2):11–22. 2016;4:11–22.
[7] Zhang Y, Jia Z, Yuan Z, Yang T, Qi Y, Zhao D. Development and application of hydrogen storage. J Iron Steel Res Int 2015;22:757–70.

[8] Jia Y, Sun C, Shen S, Zou J, Mao SS, Yao X. Combination of nanosizing and interfacial effect: future perspective for designing Mg-based nanomaterials for hydrogen storage. Renew Sustain Energy Rev 2015;44:289–303.
[9] Abbas Z, Zafar Z, Raza HH, Parveen A, Shaikh SF. Density-functional quantum analysis of optoelectronic, elastic, thermodynamic and hydrogen storage properties of AMgH3 (A= be, ca) perovskite-type hydrides: prospects for clean energy hydrogen-storage fuel and optoelectronic applications. Int J Hydrogen Energy 2024;60:212–28.
[10] Khan W. Computational screening of BeXH3 (X: Al, Ga, and In) for optoelectronics and hydrogen storage applications. Mater Sci Semicond Process 2024;174:108221.
[11] Murtaza H, Ain Q, Jbara AS, Munir J, Aldwayyan AS, Ghaithan HM, et al. The prediction of hydrogen storage capacity and solar water splitting applications of Rb2AlXH6 (X= In, Tl) perovskite halides: a DFT study. J Phys Chem Solid 2025;198:112427.
[12] Mustafa GM, Younas B, Alkhaldi HD, Mera A, Alqorashi AK, Hakami J, et al. First principle study of physical aspects and hydrogen storage capacity of magnesium-based double perovskite hydrides Mg2XH6 (X= Cr, Mn). Int J Hydrogen Energy 2024;95:300–8.
[13] Bouamrane A, Laval JP, Soulie J-P, Bastide JP. Structural characterization of NaMgH2F and NaMgH3. Mater Res Bull 2000;35:545–9.
[14] Mera A, Rehman MA. First-principles investigation for the hydrogen storage properties of AeSiH3 (Ae= Li, K, Na, Mg) perovskite-type hydrides. Int J Hydrogen Energy 2024;50:1435–47.
[15] Wang F, Liu Y, Gao M, Luo K, Pan H, Wang Q. Formation reactions and the thermodynamics and kinetics of dehydrogenation reaction of mixed alanate Na2LiAlH6. J Phys Chem C 2009;113:7978–84.
[16] Hosen A, Dahliah D, Mohammad NFA, Mousa AA, Abu-Jafar MS. A computational study on the comparative analysis of tetragonal complex metal hydride Q2FeH5 (Q= Mg, Ca, Sr) for hydrogen storage applications. Int J Hydrogen Energy 2025;102:348–59.
[17] Ayyaz A, Ullah MA, Zaman M, Alkhaldi ND, Mahmood Q, Boukhris I, et al. Investigation of hydrogen storage and energy harvesting potential of double perovskite hydrides A2LiCuH6 (A= Be/Mg/Ca/Sr): a DFT approach. Int J Hydrogen Energy 2025;102:1329–39.
[18] Ammi H, Charifi Z, Baaziz H, Ghellab T, Bouhdjer L, Adalla S, et al. Investigation on the hydrogen storage properties, electronic, elastic, and thermodynamic of Zintl Phase Hydrides XGaSiH (X= sr, ca, ba). Int J Hydrogen Energy 2024;87:966–84.
[19] Rehman MA, Rehman ZU, Usman M, Alomar SY, Khan MJ, Fatima J. Exploring the hydrogen storage in novel perovskite hydrides: a DFT study. Int J Hydrogen Energy 2024;84:447–56.
[20] Azeem W, Hussain S, Shahzad MK, Azad F, Khan G, Tirth V, et al. Computational insights of double perovskite X2CaCdH6 (X= Rb and Cs) hydride materials for hydrogen storage applications: a DFT analysis. Int J Hydrogen Energy 2024;79:514–24.
[21] Kadir K, Moser D, Munzel M, Noreus D. Investigation of Counterion Influence on an octahedral IrH6-complex in the solid state hydrides AAeIrH6 (A= Na, K and Ae= Ca, Sr, Ba, and Eu) with a new structure type. Inorg Chem 2011;50:11890–5.
[22] Giannozzi P, Baroni S, Bonini N, Calandra M, Car R, Cavazzoni C, et al. Quantum ESPRESSO: a modular and open-source software project for quantum simulations of materials. J Phys Condens Matter 2009;21:395502.
[23] Perdew JP, Burke K, Ernzerhof M. Generalized gradient approximation made simple. Phys Rev Lett 1996;77:3865.
[24] Perdew JP. Orbital functional for exchange and correlation: self-interaction correction to the local density approximation. Chem Phys Lett 1979;64:127–30.
[25] Garrity KF, Bennett JW, Rabe KM, Vanderbilt D. Pseudopotentials for high-throughput DFT calculations. Comput Mater Sci 2014;81:446–52.
[26] Heyd J, Scuseria GE. Efficient hybrid density functional calculations in solids: assessment of the Heyd–Scuseria–Ernzerhof screened Coulomb hybrid functional. J Chem Phys 2004;121:1187–92.
[27] Heyd J, Scuseria GE, Ernzerhof M. Hybrid functionals based on a screened Coulomb potential. J Chem Phys 2003;118:8207–15.
[28] Dal Corso A. Elastic constants of beryllium: a first-principles investigation. J Phys Condens Matter 2016;28:075401.
[29] Geldasa FT, Dejene FB, Kebede MA, Hone FG, Jira ET. Density functional theory study of Chlorine, Fluorine, Nitrogen, and Sulfur doped rutile TiO2 for photocatalytic application. Sci Rep 2025;15:3390.
[30] Kokalj A. XCrySDen—a new program for displaying crystalline structures and electron densities. J Mol Graph Model 1999;17:176–9.
[31] Momma K, Izumi F. VESTA 3 for three-dimensional visualization of crystal, volumetric and morphology data. J Appl Crystallogr 2011;44:1272–6.
[32] Murnaghan FD. The compressibility of media under extreme pressures, vol. 30. Proceedings of the National Academy of Sciences; 1944. p. 244–7.
[33] Birch F. Finite elastic strain of cubic crystals. Phys Rev 1947;71:809.
[34] Surucu G, Gencer A, Candan A, Gullu HH, Isik M. CaXH3 (X= Mn, Fe, Co) perovskite-type hydrides for hydrogen storage applications. Int J Energy Res 2020;44:2345–54.
[35] Mubashir M, Ali M, Bibi Z, Younis MW, Muzamil M. Efficient hydrogen storage in LiMgF3: a first principle study. Int J Hydrogen Energy 2024;50:774–86.
[36] Gencer A, Surucu G. Enhancement of hydrogen storage properties of Ca3CH antiperovskite compound with hydrogen doping. Int J Energy Res 2020;44:567–73.
[37] Ullah MA, Riaz KN, Rizwan M. Computational evaluation of KMgO3-xHx as an efficient hydrogen storage material. J Energy Storage 2023;70:108030.
[38] Manzoor A, Ullah MA, Yasin MW, Gillani SSA, Ikram M, Rizwan M. Investigation SrLiF3-xHx perovskites through ion replacement mechanism for advance solid hydrogen storage systems: a prediction through DFT-based calculations. J Energy Storage 2024;88:111639.
[39] Rizwan M, Arooj HF, Noor F, Nawaz K, Ullah MA, Usman Z, et al. Computational study to investigate effectiveness of titanium substitution in CaFeH3 perovskite-type hydride: an approach towards advanced hydrogen storage system. J Mater Res Technol 2024;31:2676–84.
[40] Broom DP, Webb CJ, Fanourgakis GS, Froudakis GE, Trikalitis PN, Hirscher M. Concepts for improving hydrogen storage in nanoporous materials. Int J Hydrogen Energy 2019;44:7768–79.
[41] Jocić M, Vukmirović N. Ab-initio calculations of temperature dependent electronic structures of inorganic halide perovskite materials. Phys Chem Chem Phys 2023;25:29017–31.
[42] Kim K, Hwang W, Oh S-HV, Soon A. Exploring anharmonic lattice dynamics and dielectric relations in niobate perovskites from first-principles self-consistent phonon calculations. npj Comput Mater 2023;9:154.
[43] Pak C-J, Jong U-G, Kang C-J, Kim Y-S, Kye Y-H, Yu C-J. First-principles study on the optoelectronic and mechanical properties of all-inorganic lead-free fluoride perovskites ABF 3 (A= Na, K and B= Si, Ge). Mater Adv 2023;4:4528–36.
[44] Zheng J, Lin C, Lin C, Hautier G, Guo R, Huang B. Unravelling ultralow thermal conductivity in perovskite Cs2AgBiBr6: dominant wave-like phonon tunnelling and strong anharmonicity. npj Comput Mater 2024;10:30.
[45] Murtaza H, Ain Q, Issa SAM, Zakaly HMH, Munir J. A precise prediction for the hydrogen storage ability of perovskite XPH3 (X= Li, Na, K) hydrides: first-principles study. Int J Hydrogen Energy 2024;94:1084–93.
[46] Mbonu IJ, Louis H, Chukwu UG, Agwamba EC, Ghotekar S, Adeyinka AS. Effects of metals (X= Be, Mg, Ca) encapsulation on the structural, electronic, phonon, and hydrogen storage properties of KXCl3 halide perovskites: perspective from density functional theory. Int J Hydrogen Energy 2024;50:337–51.
[47] Azhar U, Iftikhar MT, Arif M, Rehman MA, Ibrahim TH, El-Kadri OM. First principle investigation on the physical properties of rhodium-based XRhH3 (X= Na, Cs or Sr) perovskites hydride for hydrogen storage applications. Int J Hydrogen Energy 2025;101:1448–59.
[48] Almahmoud A, Alkhalidi H, Obeidat A. Comprehensive DFT analysis of structural, mechanical, electronic, optical, and hydrogen storage properties of novel perovskite-type hydrides Y_2CoH_6 (YCa, Ba, Mg, Sr). J Energy Storage 2025;117:116146. https://doi.org/10.1016/j.est.2025.116146.
[49] Gurunani B, Gupta DC. First-principles investigation of thermoelectric performance in KMnZ (Z= Sn, Pb) half-Heusler alloys. RSC Adv 2025;15:4874–91.
[50] Born M, Huang K. Dynamical theory of crystal lattices. Oxford university press; 1996.
[51] Firdous F, Ain Q, Issa SAM, Zakaly HMH, Munir J. A spin-polarized analysis of the half-metallicity, mechanical, structural and optoelectronic attributes of full-Heusler XVCo 2 (X= B and P) alloys. RSC Adv 2024;14:34679–89.
[52] Murtaza H, Ain Q, Munir J, Ghaithan HM, Ahmed AAA, Qaid SMH. First-principles analysis to assess the solar water splitting and hydrogen storage capabilities of Cs2XGaH6 (X= Al, Na). Int J Hydrogen Energy 2024;83:124–32.
[53] Murtaza H, Ain Q, Munir J, Ullah H, Ghaithan HM, Ahmed AAA, et al. Unveiling the mechanical, structural, thermoelectric, and optoelectronic potential of K2NaGaBr6 and K2RbTlBr6 double perovskites for sustainable technologies. Sol Energy 2024;273:112502.
[54] Zener CM, Siegel S. Elasticity and anelasticity of metals. J Phys Chem 1949;53:1468.
[55] Gurunani B, Ghosh S, Gupta DC. Comprehensive investigation of half Heusler alloy: unveiling structural, electronic, magnetic, mechanical, thermodynamic, and transport properties. Intermetallics 2024;170:108311.
[56] Andritsos EI, Zarkadoula E, Phillips AE, Dove MT, Walker CJ, Brazhkin VV, et al. The heat capacity of matter beyond the Dulong–Petit value. J Phys Condens Matter 2013;25:235401.
[57] Xu N, Song R, Zhang J, Chen Y, Chen S, Li S, et al. First-principles study on hydrogen storage properties of the new hydride perovskite XAlH3 (X= Na, K). Int J Hydrogen Energy 2024;60:434–40.
[58] Hinuma Y, Pizzi G, Kumagai Y, Oba F, Tanaka I. Band structure diagram paths based on crystallography. Comput Mater Sci 2017;128:140–84.
[59] Aroyo MI, Orobengoa D, de la Flor G, Tasci ES, Perez-Mato JM, Wondratschek H. Brillouin-zone database on the bilbao crystallographic server. Acta Crystallogr A Found Adv 2014;70:126–37.